Effect of Doping on Surface Reactivity and Conduction Mechanism in Samarium-Doped Ceria Thin Films

Nan Yang,[†,‡,∥] Alex Belianinov,[#] Evgheni Strelcov,[#] Antonello Tebano,[†,‡,§] Vittorio Foglietti,[⊥] Daniele Di Castro,[†,§] Christoph Schlueter,[▽] Tien-Lin Lee,[▽] Arthur P. Baddorf,[#] Nina Balke,[#] Stephen Jesse,[#] Sergei V. Kalinin,[#] Giuseppe Balestrino,[†,‡,§] and Carmela Aruta*[,†,‡]

[†]National Research Council CNR-SPIN, University of Roma "Tor Vergata", Rome I-00133, Italy, [‡]NAST Center, University of Roma "Tor Vergata", Rome I-00133, Italy, [§]Department DICII, University of Roma Tor Vergata, Rome I-00133, Italy, [∥]Engineering Faculty, Università degli studi Niccolò Cusano, Rome I-00166, Italy, [⊥]National Research Council, CNR-ISM Area di ricerca di Montelibretti, Monterotondo, Rome I-00016, Italy, [#]Center for Nanophase Materials Sciences, Oak Ridge National Laboratory, Oak Ridge, Tennessee 37831, United States, and [▽]Diamond Light Source Ltd., Harwell Science and Innovation Campus, Didcot OX11 0DE, United Kingdom

ABSTRACT A systematic study by reversible and hysteretic electrochemical strain microscopy (ESM) in samples of cerium oxide with different Sm content and in several working conditions allows disclosing the microscopic mechanism underlying the difference in electrical conduction mechanism and related surface activity, such as water adsorption and dissociation with subsequent proton liberation. We have measured the behavior of the reversible hysteresis loops by changing temperature and humidity, both in standard ESM configuration and using the first-order reversal curve method. The measurements have been performed in much smaller temperature ranges with respect to alternative measuring techniques. Complementing our study with hard X-ray photoemission spectroscopy and irreversible scanning probe measurements, we find that water incorporation is favored until the doping with Sm is too high to allow the presence of Ce^{3+}. The influence of doping on the surface reactivity clearly emerges from all of our experimental results. We find that at lower Sm concentration, proton conduction is prevalent, featured by lower activation energy and higher electrical conductivity. Defect concentrations determine the type of the prevalent charge carrier in a doping dependent manner.

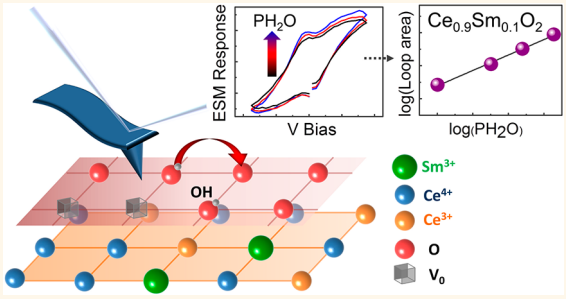

KEYWORDS: Sm-doped ceria · ion conduction · scanning probe microscopy · hard X-ray photoemission

Ceria based materials possess an interesting range of electrical transport properties. Several different conduction mechanisms are proposed in literature: electronic, protonic and oxygen ionic, depending on the temperature and doping. Namely, while pure CeO_2 is considered a bad conductor, its ionic conductivity can be increased *via* doping by trivalent rare-earth elements due to the creation of oxygen vacancies. The maximum conductivity was obtained in CeO_2 doped with Sm or Gd, *i.e.*, $Ce_{1-x}Sm_xO_2$ (SDC), which makes it an ideal electrolyte for solid oxide fuel cell applications.[1] One of the most controversial issues about ceria-based materials is its interaction with water. It has been reported that water can be incorporated into the pure ceria lattice, giving rise to proton conduction.[2] The adsorption mechanism, as well as the wetting behavior, is driven by a complex interplay of factors such as the surface morphology and the thermodynamics and kinetics associated with the adsorption. A recent atomic force microscopy study of a pure CeO_2 film showed water incorporation associated with a significant irreversible local volume deformation, demonstrating a water mediated nanowriting at room temperature.[3] In case of doped ceria, proton conduction was established in 10% Gd doped CeO_2 at temperatures below 300 °C using an electrochemical impedance spectroscopy (EIS) technique.[4] Among the possible contributions to the proton conduction in both undoped and doped ceria, a recent work elucidated the role of granularity and porosity in the water mediated conduction

* Address correspondence to carmela.aruta@spin.cnr.it.

Received for review September 20, 2014 and accepted November 21, 2014.

Published online November 21, 2014
10.1021/nn505345c

mechanism.[5] Published results are still controversial, especially because the high temperature used during the EIS measurements make it difficult to disentangle the bulk conductivity from the reaction kinetics.[6−8] Furthermore, stoichiometry and structure may change at elevated temperatures. Thus, it is difficult to disentangle these extrinsic factors from the doping-induced mechanisms related to the nature of charge carrier. In the present work, we perform measurements at lower temperature (below 110 °C) with a scanning probe microscopy technique called electrochemical strain microscopy (ESM).[9] The ESM approach is complementary to most of the studies reported in literature, where data are obtained by EIS experiments, which require the system to be in a steady state for the measured frequencies.[10] Real electrochemical systems, however, have various dynamic parameters, which cannot be easily controlled. For example, transfer of ions and energy can take place, especially upon variation of the gas environment. In addition, in the case of our thin films, the large in-plane geometry factor makes the overall impedance very high at low temperature (below 300 °C), so it is difficult to obtain reliable data by EIS. On the contrary, ESM can be readily used at lower temperatures to investigate the electrochemical systems, where the ion transfer is crucial. The chemical reaction is induced by application of a DC bias to the tip. The local defects diffuse and migrate through the material under the combined effect of the concentration gradient and electric field. The associated volume variations result in electrochemical strain[11] and the consequent dynamic surface displacement is directly detected.

Many ESM experiments show hysteretic and reversible properties without permanent volume deformation. In these situations, ESM measurements allow quantitative interpretation of hysteresis loop parameters in terms of electrochemical reactivity, which can be easily related to ion transport properties. This is the case for 10% Sm doped CeO_2 (10% SDC) and 20% Sm doped CeO_2 (20% SDC) in different temperature and humidity conditions. These two compositions are the most studied of the $Ce_{1-x}Sm_xO_2$ systems due to the high conductivity and relatively good stability in a reducing atmosphere.[12,13] On the other hand, pure CeO_2 is irreversibly deformed at room temperature and low humidity due to volume expansion,[3] which prevents studying pure CeO_2 in the same temperature and humidity range as 10% SDC and 20% SDC even with the ESM technique.

Our study is performed on epitaxial films grown on highly insulating (110) $NdGaO_3$ (NGO) substrates. Films show a remarkable structural homogeneity, as shown in the Supporting Information; therefore, the influence of microstructural features, such as grain boundaries, can be overlooked and both good reproducibility and an unambiguous interpretation of our data is established.[14]

We further explore the dynamic properties with regard to the charge carrier transport by using the first order reversal curve (FORC) mode[15] and we use unipolar voltage biased AFM to map irreversible reactions based on topographic changes as a function of air humidity. Finally, we use hard X-ray photoemission spectroscopy (HAXPES) to obtain spectroscopic data. The combination of surface electrochemical information by ESM with the voltage biased AFM, the bulk composition information and the spectroscopy data, allows us to understand the surface reaction related to the effect of Sm doping, which gives a substantial contribution on the understanding the origin of the different conducting properties in SDC.

RESULTS

Low-Temperature and Humidity Dependent Reversible and Hysteretic Electrochemical Study. ESM can probe the ionic motion and electrochemical reactions on the nanoscale depending on the working conditions and the material properties.[9] Namely, the bias applied to the tip can inject or annihilate double positively charged oxygen vacancies. As a competing mechanism, oxygen vacancies can be filled with oxygen ions or hydroxyl groups. The subsequent oxygen or proton ion movement results in a localized strain under the tip, which can be detected through dynamic surface displacement.[16] The schematics of our measurement setup is reported in Figure 1d. The voltage divider model[17] establishes the relationship between the potential drops at the junction and in the film. The low-temperature reversible electrochemical regime can be probed easily by ESM technique while being inaccessible to other methods. ESM results

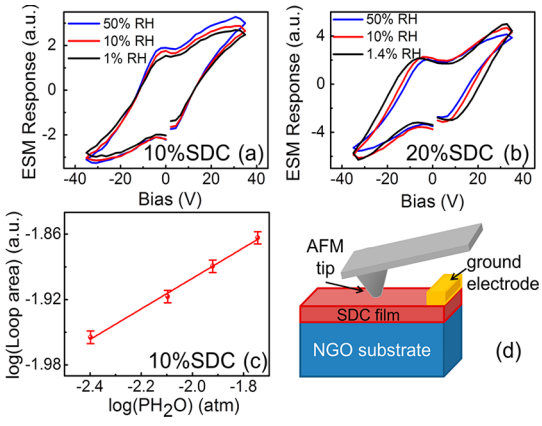

Figure 1. ESM hysteresis loops measured at three different values of relative humidity for 10% SDC (a) and for 20% SDC (b). We show only a few hysteresis loops for clarity. The logarithm of loop area as a function of the logarithm of water partial pressure for 10% SDC is reported in (c). Loops are recorded over a square grid of 10 × 10 points (1 × 1 μm^2) for each sample, and the area is averaged over the same surface. Error bars are obtained as the standard deviation of the full set of measurements. The schematic of measurement electrode setup is reported in (d).

obtained at room temperature (RT) and different humidity levels are presented in Figure 1.

The relative humidity is here converted to partial pressure of water vapor (see Supporting Information).

Since ESM signal presents an electromechanical response, it can originate from several different mechanisms: piezoelectric, Vegard strain, charge injection, surface electrochemistry, *etc*.[18] Thus, in any particular case, the measured ESM signal can be a combination of all these responses, usually with a dominant contribution from one of them. Several observations stated below suggest that we work in the electrochemical regime, where the ESM hysteretic behavior arises from the positive and negative nucleation biases (PNB and NNB) required to activate the processes of injection or annihilation of the vacancies and ions.[17] PNB and NNB are easily identified in the hysteresis loops as the voltage corresponding to the inflection points, which are related to tip−surface activation energies.[9] For the 10% SDC sample, PNB and NNB, are independent of relative humidity. Thus, in the humidity range investigated, there is no evidence of a variation in the activation energies of the involved chemical processes. On the other hand, the maximum ESM response shows a measurable variation *versus* the relative humidity (RH) and the shapes of all the hysteresis curves do not show any sign of saturation. These observations strongly support the hypothesis that the whole set of measurements of 10% SDC *vs* RH fall inside the ohmic transport region.[9,17] In this regime the transport of charged defects, *i.e.*, oxygen vacancies or protons, is linearly related the electrical conductivity of the film. Consequently, the hysteresis loop area being proportional to the change in the ion concentration beneath the tip is, in turn, proportional to film conductivity. We focused on the loop area instead of the amplitude, because the measurements can be made more accurate and reliable. Indeed, the ESM amplitude of the strain signal may suffer from drift associated errors that cannot be removed by averaging techniques. The uniform sample surface as shown in Supporting Information allows good statistics and high reproducibility, so we can plot the average of the ESM hysteresis loop area over the scanned sample surface. For 10% SDC, the loop area increases with increasing the humidity. This effect can be more clearly seen in Figure 1c, where the logarithm of loop area is plotted as a function of the water vapor pressure. In fact, on the logarithmic scale, the loop area linearly depends on water vapor. We can compare our results to the conductivity data reported in the literature:[4] the sign of the slope is considered as a fingerprint of the type of conduction mechanism. Namely, the positive slope for 10% SDC indicates a prevalently protonic conduction mechanism. The data related to 20% SDC film show hysteresis loop with a sizable variation of the PNB and NNB in the range of humidity experimentally investigated, giving evidence

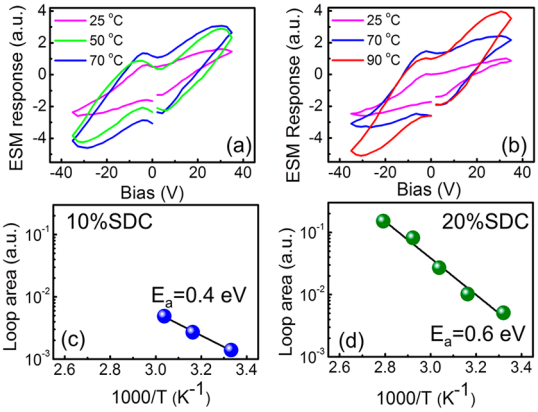

Figure 2. ESM hysteresis loops obtained at three different temperatures for 10% SDC (a) and 20% SDC (b). We show only a few hysteresis loops for clarity. Arrhenius plot of the loop area for 10% SDC (c) and 20% SDC (d). Loops are recorded over a square grid of 10 × 10 points (1 × 1 μm^2) for each sample, and the area is averaged over the surface. The temperature range in panel c is narrower because 10% SDC starts to deform above the highest temperature shown in the plot. Therefore, only three significative data points could be reported in the figure.

of a variation of the activation energies. This result can be ascribed to activated processes acting in parallel, the process with lower activation energy prevailing at high relative humidity. In this case, the presence of multiple activated processes does not allow establishing a simple proportionality relationship between the hysteresis loop area and the electrical conductivity. We further explore the temperature dependence of ESM response to estimate the activation energy of the transport process.[19] 10% SDC and 20% SDC samples were measured at various temperatures in air with 50% RH. The ESM hysteresis loops reported in Figure 2 show an increase of the loop area with increasing temperature for both samples. The PNB and NNB values are independent of temperature and the whole set of measurements of 10% SDC and 20% SDC fall inside the ohmic transport region. In this regime the hysteresis loop area for both samples is proportional to the ion conductivity. The increase of the ESM loop area is due to the thermal activation effect on ionic and protonic mobility, depending on prevalent charge carrier type. Therefore, the Arrhenius plot can allow estimating the activation energy for the transport process. The results reported in Figure 2c,d show a linear behavior. An activation energy of about 0.4 and 0.6 eV, for 10% SDC and 20% SDC sample, respectively, is obtained in agreement with macroscopic measurements reported in literature.[4,12] Such values are usually associated with the different conduction mechanisms, namely protonic and ionic mechanisms in 10% SDC and 20% SDC, respectively.

Transport Mechanism Investigation by First Order Reversal Curve Measurements. To get further insight into the microscopic mechanisms inferred above, first order reversal curve (FORC) measurements were performed at two different humidity levels, namely, in dry air

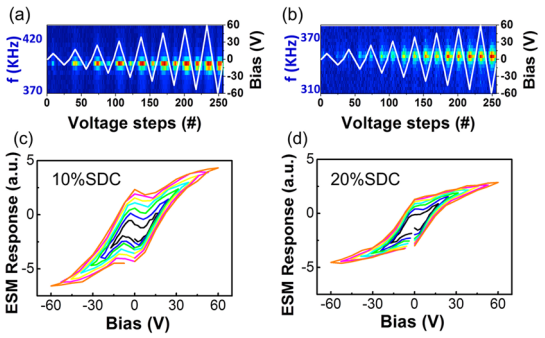

Figure 3. FORC-type ESM measurements in wet conditions on 10% SDC film in panels a and c and 20% SDC in panels b and d. 2D plot of the amplitude spectra of the cantilever resonance response in 10% SDC (a) and 20% SDC (b) as a function of the DC bias spectrum reported in the same graph (white line). Average loops over a square grid of 10 × 10 points (1 μm × 1 μm) measured in 10% SDC (c) and in 20% SDC (d). Note that the frequency ranges in plots a and b are different but with the same interval width.

(approximately 1% RH) and wet air (50% RH) at RT.[20,21] FORC is a powerful tool to study the on-site transport process for a typical electrochemical reaction-diffusion system. It consists in progressively increasing the peak bias voltage V_p of the ESM measurements, thus allowing systematic tracing of the evolution of loops.[22]

Considering that our thin films are mixed ionic and electronic conductor,[23] the measurement is performed with tip and ground electrode (see Figure 1d) separated at a distance of several hundreds of microns. This experimental setup will enable a very high dynamic range in our measurements, over 120 V sweep, where most of the voltage drop is located longitudinally along the film. Differently from the configuration suited for applications, where leads are not put sideways and the current ion direction is mainly perpendicular to the surface,[24,25] our setup is optimized to investigate the nature of the ionic transport properties, where both ions and electrons move longitudinally parallel to the surface. Detailed numerical calculations would be required to estimate the exact contributions of the different transport mechanisms.[24,25]

In Figure 3, we present FORC ESM results obtained in the presence of humidity for 10% SDC and 20% SDC. In addition to the ESM signal measurement, also the changes in resonance frequency, obtained in band excitation mode, have been measured.[26] The evolution of the resonance frequency is shown in Figure 3, panels a and b for 10% SDC and 20% SDC, respectively. The resonance frequency gives direct information about the changes in mechanical properties of the tip–surface junction, which can depend on friction, viscous flow, and plastic deformation, eventually mediated by the local wetting.[27] In particular, the presence of water menisci strongly affects the contact adhesion force between the AFM tip and the sample surface.[28] The enhanced surface interaction force experienced by the tip acts as in the presence of a larger elastic

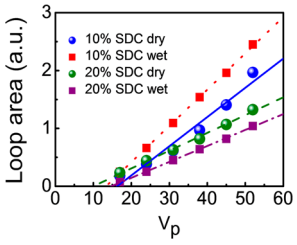

Figure 4. Loop-area *vs* peak bias voltage V_p for both 10% SDC and 20% SDC samples and both in dry and wet conditions. The FORC-type ESM data and the fits correspond exclusively to the linear regions.

modulus of the material, thus increasing the resonance frequency.[29] Namely, while the resonance frequency is similar between the two samples when measured in dry conditions (see Supporting Information), a change occurs in wet conditions, depending on the Sm concentration: in the case of 20% SDC the resonance frequency increases from about 330 kHz in dry atmosphere, up to about 340 kHz in wet atmosphere, while, in the case of 10% SDC, it increases from about 350 kHz in dry, up to about 385 kHz in wet atmosphere. In agreement, the quality factor decreases when the resonance frequency increases. The higher value in the presence of water for 10% SDC can be explained in terms of greater hydrophilic properties.

In Figure 3c,d, we report the ESM signal hysteresis loops in wet conditions. The loops progressively open up with increasing bias voltage. The positive or negative nucleation biases do not vary with changing the bias voltage. The same occurs for the hysteresis loops measured in dry conditions, as reported in Supporting Information.

At higher values of V_p, above the critical voltage needed for the activation of the electrochemical reaction process, the measurements of loop area is linearly related to the excitation bias. The slope *b* is related to the electrical conductivity of the film[22] and represents the ratio of the loop area and the peak bias voltage variation, Δ(Loop_Area) and ΔV_p:

$$b = \frac{\Delta(\text{Loop\_Area})}{\Delta V_p} \quad (1)$$

Above the critical voltage needed for the activation of the electrochemical reaction process, the ESM signal can be fitted well. This region corresponds to the ohmic transport region where the hysteresis loop area is proportional to the change in the film conductivity. Figure 4 shows the plot of the loop area corresponding to the linear regions *versus* the maximum excitation bias V_p for both of the samples in dry and wet air. The linear fit gives the slope of the fitting lines (*b* parameter). Because of the assumption that our data fall inside the ohmic transport region, the slope *b* is proportional to the electrical conductivity of the film. With this assumption, Figure 4 shows very interesting features, which were hidden in the case of measurements

of single hysteresis loops (see Figure 1). Now we can compare data independently from the different chemical activated processes. Figure 4 shows a higher slope for 10% SDC data as compared to 20% SDC, which is in agreement with larger mobility of protons with respect to oxygen ions.[30] The higher mobility can be also explained by the larger voltage drop inside the sample due to the presence of water menisci. We cannot discriminate between the two effects, but the conclusions are not altered because a larger slope is observed in 10% SDC than in 20% SDC sample. Moreover, the slope of the data of the 10% SDC sample is higher in the wet conditions with respect to the dry conditions, in agreement with the data shown in Figure 1c and consistent with a change in the carrier concentration. On the other hand, the slope of the data of the 20% SDC sample does not show any change *versus* relative humidity. This behavior will be discussed later.

Irreversible Volume Deformation. To establish the reactivity of SDC, the effect of humidity was also investigated by biasing the samples with a unipolar voltage waveform through the AFM conducting tip. The sample surface was mapped with +35 V DC bias applied to the tip at a scanning rate of 0.2 s/line. By increasing RH of the air gas blowing through the measurement chamber at room temperature, a very small volume expansion of less than a nanometer was initially observed for the 10% SDC film, but no measurable expansion was observed for the 20% SDC. Such an expansion was suddenly observed for the 10% SDC sample as soon as the measuring temperature was increased above 80 °C as shown in Figure 5b. A similar irreversible expansion was reported for pure CeO_2 already starting from room temperature[3] as shown in Figure 5a. As it can be observed in Figure 5c, the volume deformation for 10% SDC increases when RH is varied in the range 10−50% . This finding can be considered as a direct proof of the presence of OH groups, originating from the water droplet at the tip−surface junction, which OH groups fill the oxygen vacancies irreversibly. This behavior is similar to the water-mediated nanowriting electrochemical mechanism observed on pure CeO_2.[3] However, whereas for pure CeO_2 film, the expansion was observed even at room temperature (Figure 5a), a higher temperature is required for the 10% SDC film to activate the water adsorption and proton formation, indicating that 10% of doping with Sm in SDC starts to inhibit the efficiency of such a process. Indeed, the water adsorption and proton formation is completely inhibited by further increasing of dopant concentration to 20% at the same temperature.

Hard X-ray Photoelectron Spectroscopy Study. Finally, to complement our study, we measured bulk spectroscopic properties by HAXPES to correlate these data with the surface sensitive information reported in previous sections. In fact, as a result to the high incident

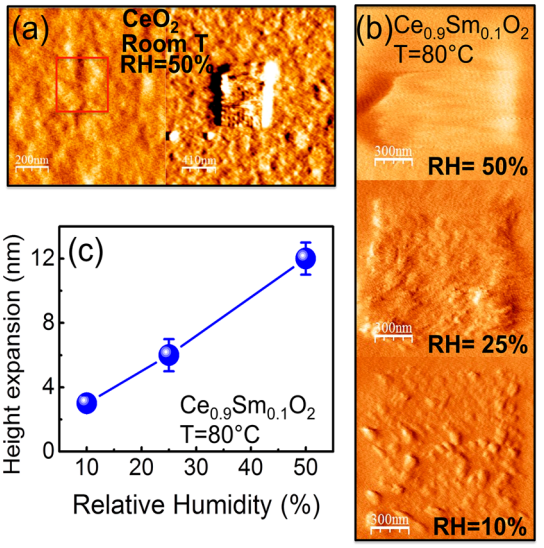

Figure 5. (a) AFM deflection images of the CeO2 surface before (left) and after (right) mapping with +15 V DC bias. The measurements were performed at room temperature and 50% relative humidity RH. Maximum height of deformation is about 20 nm. (b) AFM deflection images at different RH for the 10% SDC sample. The bias applied to the tip is +35 V. (c) Plot of the average volume expansion as a function of RH. The measurements were performed at T = 80 °C.

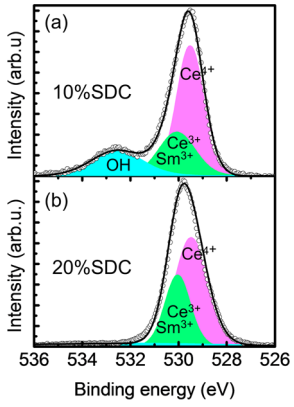

Figure 6. O 1s core level HAXPES spectra for 10% SDC in (a) and 20% SDC in (b). Experimental data (open circles) are compared with the fit results (solid black line), obtained as the envelope of the fit curve components reported in the panels as filled areas [cyan (OH), magenta (Ce^{4+}), and green (Ce^{3+} and Sm^{3+})] under the curves.

energy of 6.054 keV, HAXPES measurements are quite bulk-sensitive (the probing depth was about 20 nm) and the surface contaminant contribution to the spectra is less relevant than in case of soft X-rays. O 1s core level spectra for 10% SDC and 20% SDC are shown in Figure 6. Two main differences must be noticed between the two samples. The highest peak of the spectra is shifted to lower binding energy in the 10% SDC (Figure 6a) with respect to the 20% SDC (Figure 6b), from 529.8 to 529.5 eV. More interestingly, an additional peak is present at about 532.5 in the 10% SDC film, which can be attributed to the hydroxyl OH groups formed because of the water trapped during the

previous ESM measurements performed in wet conditions.[31] No relevant OH content can be detected in the 20% SDC film. Data were fitted by keeping the number of components at minimum and fixing their binding energy at the same value for both samples. We can identify two main components of the leading peak, associated with the structural oxygen ions in two different SDC lattice sites. The component at lower binding energy can be associated with the structural oxygen bonded to Ce^{4+}, while the component at higher binding energy with the structural oxygen bonded to Ce^{3+} or Sm^{3+}. Assuming the nominal concentration for Sm^{3+}, we conclude that the Ce^{3+} content is lower in 20% SDC than in 10% SDC (see Supporting Information).

DISCUSSION AND CONCLUSIONS

It is generally accepted that pure CeO_2 can be easily reduced to nonstoichiometric CeO_{2-x}.[32] The consequent formation of Ce^{3+} mainly compensates for the formation of positively charged oxygen vacancies. The process of CeO_2 reduction in the Kroger-Vink notation can be written as

$$2Ce_{Ce}^{x} + O_O^{x} \rightarrow 2Ce_{Ce}' + V_O^{\bullet\bullet} + \frac{1}{2}O_2 \qquad (2)$$

where Ce_{Ce}^{x} and O_O^{x} are the Ce^{4+} and the O^{2-} in the normal lattice, Ce_{Ce}' is the Ce^{3+} having one less positive charge compared to the Ce^{4+}, $V_O^{\bullet\bullet}$ is the double positively charged oxygen vacancy, and O_2 is the molecular oxygen. In SDC, oxygen vacancies are introduced by doping with trivalent metal oxide, using Sm_2O_3:

$$Sm_2O_3 \xrightarrow{CeO_2} 2Sm_{Ce}' + V_O^{\bullet\bullet} + 3O_O^{x} \qquad (3)$$

where $Sm^{3+}$is hosted in the Ce^{4+} lattice site with one less positive charge, *i.e.*, Sm_{Ce}' in Kroger-Vink notation. Oxygen vacancies are then formed to compensate for the charge imbalance. Moreover, reaction 2 can also take place in SDC, where the concomitant Sm doping by reaction 3 will naturally affect the equilibrium of the first reaction. In fact, the amount of Ce^{3+} will obviously be decreased due to the Sm^{3+} substitution in its lattice site. A lower Ce^{3+} content with increasing the Sm^{3+} substitution is actually observed in HAXPES measurements from O 1s and Ce 3d core level spectra, as reported in Supporting Information: Ce^{3+} concentration is almost reduced by a half when the Sm concentration is doubled.

It is known that the surface of CeO_2 oxide is catalytically active and a variety of molecules, including water, can be trapped there.[33] Very recently the electrochemical reactions of these mixed conductors have been investigated at the surface-gas interface during hydrogen oxidation and water splitting.[34]

Ce^{3+} and oxygen vacancies are believed to be the active sites in the following hydrogen evolution reaction:[35,32]

$$H_2O + Ce_{Ce}' + V_O^{\bullet\bullet} \rightarrow OH^{\bullet} + Ce_{Ce}^{x} + \frac{1}{2}H_2 \qquad (4)$$

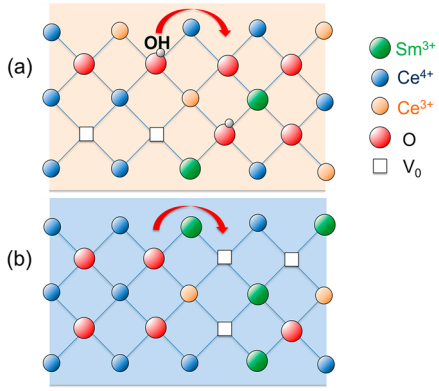

Figure 7. Schematic representation of the conduction mechanism for 10% SDC (a) and 20% SDC (b).

In our experimental setup, the reactions are electrochemically driven in wet gas phase. In the above reaction the water splitting is located at the cathode electrode and the cerium oxidation reaction at the anode electrode. In the chosen measuring system, the electrodes (shown in Figure 1d) are on the same side of the film and are exposed to the same identical gas phase conditions. In these experimental condition reversing the electrodes does not reverse the oxidation–reduction reaction, because of the presence of water on both electrodes. Cerium will be oxidized until a sufficient concentration of Ce^{3+} is available; thus reaction 4 will proceed irreversibly filling the oxygen vacancies with $OH^{\bullet}$. A lower amount of Ce^{3+}, *i.e.*, Ce_{Ce}' in Kroger-Vink notation, will reduce the rate of the above reaction, thus with the increase of Sm doping concentration the following oxygen evolution/reduction reactions will become the dominant mechanism:

$$O_O^{x} \Leftrightarrow V_O^{\bullet\bullet} + 2e + \frac{1}{2}O_2 \qquad (5)$$

The whole set of experimental results can be explained in the light of these two prevalent reactions. The different behavior of 10% SDC and 20% SDC originates from the Sm doping concentrations, which affect the Ce^{3+} content. In the case of 10% SDC, water dissociation proceeds due to the presence of the active Ce^{3+} yielding hydroxyl groups, which fill some of the oxygen vacancies. This is supported by HAXPES measurements at the O 1s core level of Figure 6, showing the presence of hydroxyls group in 10% SDC film and not in 20% SDC. Hydroxyl groups can be localized or give rise to proton conduction by hopping on oxygen sites, as schematically shown in Figure 7a. In contrast, doping with Sm above 10% enhances the stability of Ce^{4+} and the main chemical process is the oxygen evolution/reduction reaction of eq 5. The concomitant local distortion, induced near the oxygen vacancy by the bigger size of Sm ion and longer bond length, favors the oxygen mobility, since the so-called mechanochemical coupling largely affect the energy barrier for oxygen migration.[36,37] For 20% SDC, ion

conduction process is prevalent, as schematically shown in Figure 7b.

In the ESM measurements, the surface displacement is driven by the generation/annihilation of electroactive species (oxygen vacancies, protons, hydroxyls) at the tip−surface junction with subsequent diffusion or migration driven transport through the film. In the humidified air condition, when an external electric field is applied to the film surface, both water splitting and oxygen reduction reaction can occur. The presence of oxygen vacancies allows both OH or oxygen atoms to enter (reactions 4 or 5), but the valence of Ce needs to change accordingly to preserve the neutrality of the system. As a matter of fact, oxygen vacancies can be filled by OH or oxygen depending on the vacancy concentration, the Sm and Ce content, and Ce valence (Ce^{3+}/Ce^{4+}). With an increasing ambient humidity, increasingly more OH groups are formed according to reaction 4. Therefore, ESM measurements with different humidity allow to elucidate if the prevalent chemical reaction is mediated by OH or oxygen ions. The mobile charge carriers will diffuse under the concentration gradient.[14] Since the ESM hysteresis loop is proportional to the change in the ion concentration and, in turn, to the film conductivity,[9] an increase of the loop area is expected with increasing the water partial pressure, when the prevalent charge carrier type is of proton nature.

The ESM measurements reported in Figures 1 and 4 show that the conductivity increases with the water partial pressure in the case of 10% SDC, while the transport properties are not affected by water in the case of 20% SDC. We can deduce that the prevalent charge carrier type is the proton in 10% SDC, while it is the oxygen ion in 20% SDC. The main conduction mechanisms observed for the two samples in the temperature and humidity range we examined, by protons in 10% SDC (lower Sm doping) and by oxygen ions in 20% SDC (higher Sm doping), are consistent with the reactions of eqs 4 and 5. The observation of the volume expansion shown in Figure 5 for 10% SDC, which is strongly dependent on the relative humidity, is consistent with the irreversible nature of reaction 4. In conclusion, our investigation demonstrates the role of Sm doping in the surface reactions and the type of charge carrier prevalent in the conduction. The doping strongly influences the channel reactions; the trivalent doping element concentration must be considered as an important factor for the design of ceria-based systems and of doped solid oxides in general, a factor that can help improve applications in energy storage devices.

METHODS

Thin Film Deposition. $Ce_{0.9}Sm_{0.1}O_2$ (10% SDC) and $Ce_{0.8}Sm_{0.2}O_2$ (20% SDC) epitaxial thin films were grown by Pulsed Laser Deposition technique on an insulating (110) $NdGaO_3$ substrate having a thickness of 300 nm. The KrF excimer pulsed laser source (λ = 248 nm) was operated at 10 Hz, with an energy density of 5 J/cm^2; the substrate temperature was about 600 °C; the oxygen partial pressure was 5 Pa and target-to-substrate distance was 3.5 cm. With this set of parameters, a deposition rate of about 0.22 Å per laser shot was obtained.

XRD Characterizations. XRD analysis was performed on SDC films to determine the lattice parameters and to rule out the presence of impurity phases. A Rigaku D-max diffractometer was used in the $\theta - 2\theta$ mode and rocking curves using Cu Kα radiation, accelerating voltage of 30 kV, filament current of 30 mA, 2 deg/min (scan rate for the $\theta - 2\theta$ scan), 0.5 deg/min (scan rate for the θ-scan).

ESM Spectroscopy. The electrochemical activity of SDC films was investigated as a function of relative air humidity in the range between 1% to about 80% . The experiments under controlled humidity were performed on an ambient commercial atomic force microscope system (Bruker Multimode 8) equipped with a LabVIEW/Matlab based band excitation software for voltage and time spectroscopies.[38] An environmental cell (measurement chamber) connected to an air tank through a humidifier (General Electric) was used for humidity measurement. The sample temperature was changed by a heating stage (Bruker) and was stabilized by waiting for at least 15 min at each temperature set point.[39]

HAXPES. The HAXPES measurements were performed at the beamline I09 at the Diamond Light Source, U.K. using a photon energy of 6.054 keV. A channel-cut Si (004) crystal was employed after the primary double crystal monochromator to achieve an energy resolution of <250 meV, while maintaining a high photon flux. Photoelectron spectra were measured with a EW4000 photoelectron analyzer (VG Scienta, Uppsala, Sweden) mounted in the polarization direction of the photon beam. Count rates were maximized by tuning the incident angle to about 1°. Photoemission measurements were performed at 400 K, the binding energy scale was calibrated to the Fermi edge cutoff of an Au reference sample.

Conflict of Interest: The authors declare no competing financial interest.

Acknowledgment. The authors acknowledge META—Materials Enhancement for Technological Applications Project (FP7-PEOPLE-2010-IRSES—Marie Curie Actions, PIRSES-GA-2010-269182). Italian MIUR is acknowledged for support through the FIRB Project RBAP115AYN *"Oxides at the nanoscale: multifunctionality and applications"* and PRIN Project 2010-2011 OXIDE, *"OXide Interfaces: emerging new properties, multifunctionality, and Devices for Electronics and Energy"*. The SPM part of this research was conducted at the Center for Nanophase Materials Sciences, which is a DOE Office of Science User Facility (user project CNMS2014-046).

Supporting Information Available: Additional experimental results on XRD, AFM, FORC, and HAXPES. This material is available free of charge *via* the Internet at http://pubs.acs.org.

REFERENCES AND NOTES

1. Ruiz-Trejo, E.; Sirman, J. D.; Baikov, Y. M.; Kilner, J. A. Oxygen Ion Diffusivity, Surface Exchange and Ionic Conductivity in Single Crystal Gadolinia Doped Ceria. *Solid State Ionics* **1998**, *113*, 565–569.
2. Yokokawa, H.; Horita, T.; Sakai, N.; Yamaji, K.; Brito, M. E.; Xiong, Y.-P.; Kishimoto, H. Protons in Ceria and Their Roles in SOFC Electrode Reactions from Thermodynamic and SIMS Analyses. *Solid State Ionics* **2004**, *174*, 205–221.
3. Yang, N.; Doria, S.; Kumar, A.; Jang, J. H.; Arruda, T. M.; Tebano, A.; Jesse, S.; Ivanov, I. N.; Baddorf, A. P.; Strelcov, E.;

et al. Water-Mediated Electrochemical Nano-Writing on Thin Ceria Films. *Nanotechnology* **2014**, *25*, 075701–075708.
4. Ruiz-Trejo, E.; Kilner, J. A. Possible Proton Conduction in $Ce_{0.9}Gd_{0.1}O_{2-\delta}$ Nanoceramics. *J. Appl. Electrochem.* **2009**, *39*, 523–528.
5. Gregori, G.; Shirpour, M.; Maier, J. Proton Conduction in Dense and Porous Nanocrystalline Ceria Thin Films. *Adv. Funct. Mater.* **2013**, *23*, 5861–5867.
6. Zha, S.; Xia, C.; Meng, G. Effect of Gd (Sm) Doping on Properties of Ceria Electrolyte for Solid Oxide Fuel Cells. *J. Power Sources* **2003**, *115*, 44–48.
7. Yahiro, H.; Eguchi, Y.; Eguchi, K.; Arai, H. Oxygen Ion conductivity of the Ceria-Samarium Oxide System with Fluorite Structure. *J. Appl. Electrochem.* **1988**, *18*, 527–531.
8. Takamura, H.; Takahashi, N. Electrical Conductivity of Dense Nanocrystalline Ceria under Humidified Atmosphere. *Solid State Ionics* **2010**, *181*, 100–103.
9. Kumar, A.; Ciucci, F.; Morozovska, A. N.; Kalinin, S. V.; Jesse, S. Measuring Oxygen Reduction/Evolution Reactions on the Nanoscale. *Nat. Chem.* **2011**, *3*, 707–713.See also Supporting Information .
10. Gabrielli, C. *Identification of Electrochemical Process by Frequency Response Analysis*, Monograph Reference 004 /83, Solartron Instr.Group: Farnsborough, England, 1980.
11. Bishop, S. R.; Duncan, K. L.; Wachsman, E. D. Defect Equilibria and Chemical Expansion in Non-Stoichiometric Undoped and Gadolinium-Doped Cerium Oxide. *Electrochim. Acta* **2009**, *54*, 1436–1443.
12. Sanna, S.; Esposito, V.; Pergolesi, D.; Orsini, A.; Tebano, A.; Licoccia, S.; Balestrino, G.; Traversa, E. Fabrication and Electrochemical Properties of Epitaxial Samarium-Doped Ceria Films on $SrTiO_3$-Buffered MgO Substrates. *Adv. Funct. Mater.* **2009**, *19*, 1713–1719.
13. Kharton, V. V.; Figueiredo, F. M.; Navarro, L.; Naumovich, E. N.; Kovalevsky, A. V.; Yaremchenko, A.; Viskup, A. P.; Carniero, A.; Marques, F. M. B.; Frade, J. R. Ceria-Based Materials for Solid Oxide Fuel Cells. *J. Mater. Sci.* **2001**, *36*, 1105–1117.
14. Doria, S.; Yang, N.; Kumar, A.; Jesse, S.; Tebano, A.; Aruta, C.; Di Bartolomeo, E.; Arruda, T. M.; Kalinin, S. V.; Licoccia, S.; *et al.* Nanoscale Mapping of Oxygen Vacancy Kinetics in Nanocrystalline Samarium Doped Ceria Thin Films. *Appl. Phys. Lett.* **2013**, *103*, 171605–171608.
15. Vasudevan, R. K.; Marincel, D.; Jesse, S.; Kim, Y.; Kumar, A.; Kalinin, S. V.; Trolier-McKinstry, S. Polarization Dynamics in Ferroelectric Capacitors: Local Perspective on Emergent Collective Behavior and Memory Effects. *Adv. Funct. Mater.* **2013**, *23*, 2490–2508.
16. Morozovska, A. N.; Eliseev, E. A.; Balke, N.; Kalinin, S. V. Local Probing of Ionic Diffusion by Electrochemical Strain Microscopy: Spatial Resolution and Signal Formation Mechanisms. *J. Appl. Phys.* **2010**, *108*, 053712–053732.
17. Kumar, A.; Ciucci, F.; Leonard, D.; Jesse, S.; Biegalski, M.; Christen, H.; Mutoro, E.; Crumlin, E.; Shao-Horn, Y.; Borisevich, A.; *et al.* Probing Bias-Dependent Electrochemical Gas−Solid Reactions in $(La_xSr_{1-x})CoO_{3-\delta}$ Cathode Materials. *Adv. Funct. Mater.* **2013**, *23*, 5027–5036.
18. Balke, N.; Maksymovych, P.; Jesse, S.; Kravchenko, I. I.; Li, Q.; Kalinin, S. V. Exploring Local Electrostatic Effects with Scanning Probe Microscopy: Implications for Piezoresponse Force Microscopy and Triboelectricity. *ACS Nano* **2014**, *8*, 10229–10236.
19. Balke, N.; Kalnaus, S.; Dudney, N. J.; Daniel, C.; Jesse, S.; Kalinin, S. V. Local Detection of Activation Energy for Ionic Transport in Lithium Cobalt Oxide. *Nano Lett.* **2012**, *12*, 3399–3403.
20. Mayergoyz, I. D. *Mathematical Models of Hysteresis*; Springer-Verlag: New York, 1990.
21. Kumar, A.; Ovchinnikov, O. S.; Funakubo, H.; Jesse, S.; Kalinin, S. V. Real-Space Mapping of Dynamic Phenomena During Hysteresis Loop Measurements: Dynamic Switching Spectroscopy Piezoresponse Force Microscopy. *Appl. Phys. Lett.* **2011**, *98*, 202903–202905.
22. Balke, N.; Jesse, S.; Kim, Y.; Adamczyk, L.; Ivanov, I. N.; Dudney, N. J.; Kalinin, S. V. Decoupling Electrochemical Reaction and Diffusion Processes in Ionically Conductive Solids on the Nanometer Scale. *ACS Nano* **2010**, *4*, 7349–7357.
23. Chueh, W. C.; Lai, W.; Haile, S. M. Electrochemical Behavior of Ceria with Selected Metal Electrodes. *Solid State Ionics* **2008**, *179*, 1036–1041.
24. Ciucci, F.; Chueh, W. C.; Goodwin, D. G.; Haile, S. M. Surface Reaction and Transport in Mixed Conductors with Electrochemically-Active Surfaces: A 2-D Numerical Study of Ceria. *Phys. Chem. Chem. Phys.* **2011**, *13*, 2121–2135.
25. Chen, C.; Chen, D.; Chueh, W. C.; Ciucci, F. Modeling the Impedance Response of Mixed-Conducting Thin Film Electrodes. *Phys. Chem. Chem. Phys.* **2014**, *16*, 11573–11583.
26. Jesse, S.; Kalinin, S. V.; Proksch, R.; Baddorf, A. P.; Rodriguez, B. J. The Band Excitation Method in Scanning Probe Microscopy for Rapid Mapping of Energy Dissipation on the Nanoscale. *Nanotechnology* **2007**, *18*, 435503–435510.
27. Stark, M.; Stark, R. W.; Heckl, W. M.; Guckenberger, R. Inverting Dynamic Force Microscopy: from Signals to Time-Resolved Interaction Forces. *Proc. Natl. Acad. Sci. U.S.A.* **2002**, *99*, 8473–8478.
28. Sirghi, L.; Szoszkiewicz, R.; Riedo, E. Volume of a Nanoscale Water Bridge. *Langmuir* **2006**, *22*, 1093–1098.
29. Lucas, M.; Mai, W.; Yang, R.; Wang, Z. L.; Riedo, E. Aspect Ratio Dependence of the Elastic Properties of ZnO Nanobelts. *Nano Lett.* **2007**, *7*, 1314–1317.
30. Solís, C.; Escolastico, S.; Haugsrud, R.; Serra, J. M. $La_{5.5}WO_{12-\delta}$ Characterization of Transport Properties under Oxidizing Conditions: A Conductivity Relaxation Study. *J. Phys. Chem. C* **2011**, *115*, 11124–11131.
31. Chen, Q.; El Gabaly, F.; Akgul, F. A.; Liu, Z.; Mun, B. S.; Yamaguchi, S.; Braun, A. Observation of Oxygen Vacancy Filling under Water Vapor in Ceramic Proton Conductors *in Situ* with Ambient Pressure XPS. *Chem. Mater.* **2013**, *25*, 4690–4696.
32. Trovarelli, A. Catalytic Properties of Ceria and CeO_2-Containing Materials. *Catal. Rev. Sci. Eng.* **2006**, *38*, 439–520.
33. Trovarelli, A.; de Leitenburg, C.; Boaro, M.; Dolcetti, G. The Utilization of Ceria in Industrial Catalysis. *Catal. Today* **1999**, *50*, 353–367.
34. Feng, A. Z.; El Gabaly, F.; Ye, X.; Shen, Z.-X.; Chueh, W. C. Fast Vacancy-Mediated Oxygen Ion Incorporation Across the Ceria−Gas Electrochemical Interface. *Nat. Commun.* **2014**, *5*, 4374–4382.
35. Chueh, W. C.; McDaniel, A. H.; Grass, M. E.; Hao, Y.; Jabeen, N.; Liu, Z.; Haile, S. M.; McCarty, K. F.; Bluhm, H.; El Gabaly, F. Highly Enhanced Concentration and Stability of Reactive Ce^{3+} on Doped CeO_2 Surface Revealed in Operando. *Chem. Mater.* **2012**, *24*, 1876–1882.
36. Ahn, K.; Yoo, D. S.; Prasad, D. H.; Lee, H.-W.; Chung, Y.-C.; Lee, J.-H. Role of Multivalent Pr in the Formation and Migration of Oxygen Vacancy in Pr-Doped Ceria: Experimental and First-Principles Investigations. *Chem. Mater.* **2012**, *24*, 4261–4267.
37. Yildiz, B. Stretching" the Energy Landscape of Oxides—Effects on Electrocatalysis and Diffusion. *MRS Bull.* **2014**, *39*, 147–156.
38. Jesse, S.; Maksymovych, P.; Kalinin, S. V. Rapid Multidimensional Data Acquisition in Scanning Probe Microscopy Applied to Local Polarization Dynamics and Voltage Dependent Contact Mechanics. *Appl. Phys. Lett.* **2008**, *93*, 112903–112905.
39. Kumar, A.; Jesse, S.; Morozovska, A. N.; Eliseev, E.; Tebano, A.; Yang, N.; Kalinin, S. V. Variable Temperature Electrochemical Strain Microscopy of Sm-Doped Ceria. *Nanotechnology* **2013**, *24*, 145401.